

The Panchromatic Hubble Andromeda Treasury XX: Ages and Masses of the Year 1 Stellar Clusters

Morgan Fouesneau¹, L. Clifton Johnson¹, Da² R. Weisz¹, Julianne J. Dalcanton¹, Eric F. Bell², Dimitrios A. Gouliermis^{3,4} Søren S. Larsen⁵, Puragra Guhathakurta⁶, Jason Kalirai⁷, Hans-Walter Rix⁴, Anil C. Seth⁸, Evan D. Skillman⁹, and Benjamin F. Williams¹

mfouesn@astro.washington.edu

Received _____; accepted _____

¹Department of Astronomy, University of Washington, Seattle, Washington, USA

²Department of Astronomy, University of Michigan, 500 Church Street, Ann Arbor, MI 48109, USA

³Institut für Theoretische Astrophysik, Zentrum für Astronomie der Universität Heidelberg, Albert-Ueberle-Strasse 2, 69120 Heidelberg, Germany

⁴Max-Planck-Institut für Astronomie, Königstuhl 17, 69117 Heidelberg, Germany

⁵Department of Astrophysics, IMAPP, Radboud University Nijmegen, P.O. Box 9010, 6500 GL Nijmegen, The Netherlands

⁶University of California Observatories/Lick Observatory, University of California, 1156 High Street, Santa Cruz, CA 95064, USA

⁷Space Telescope Science Institute, 3700 San Martin Drive, Baltimore, MD 21218, USA

⁸Department of Physics and Astronomy, University of Utah, Salt Lake City, UT 84112, USA

⁹Department of Astronomy, University of Minnesota, 116 Church Street SE, Minneapolis, MN 55455, USA

ABSTRACT

We present the ages and masses for 601 star clusters in M31 from the analysis of the six filter integrated light measurements made as part of the Panchromatic Hubble Andromeda Treasury (PHAT). We derive the ages and masses for clusters using a probabilistic technique that accounts for the effects of stochastic sampling of the stellar mass function. Combined with the exquisite sensitivity of the PHAT observations and their broad wavelength baseline, this method provides robust age and mass recovery for clusters ranging from $\sim 10^2 - 2 \times 10^6 M_{\odot}$.

We find that the cluster age distribution is roughly uniform over the past 100 Myr in broad agreement with previous studies. The age distribution of older (> 100 Myr) clusters is consistent with a power law of index -1.1 . We find that the mass distribution of the whole sample can be well-described by a single power-law with a spectral index of -1.9 ± 0.1 over the range of $10^3 - 3 \times 10^5 M_{\odot}$. However, if we subdivide the sample by galactocentric radius, we find that the mass spectral index varies significantly, with best fits values between -2.2 and -1.8 , while the age distributions remains unchanged. Thus, this analysis suggests that the cluster mass function may vary with respect to environment.

Subject headings: Galaxies: Individual (M31), Star clusters — Methods: data analysis, statistical — Techniques: photometric

1. Introduction

Star clusters have been our main key to understanding stellar evolution for many decades. While clusters continue to provide precious constraints on stellar physics, they are studied in their own right today and serve as tracers of the histories of galaxies. It

has become clear that a significant fraction of star formation occurs in clusters and that events such as galaxy interactions can trigger their formation (e.g., spiral arms, interactions; Meurer et al. 1995; Barton et al. 2000; Di Matteo et al. 2007). However, understanding galaxy histories from observations of clusters is complicated by uncertainties. Questions have been raised regarding cluster properties in various environments, the systematic trends in their color distributions, their lifetimes as gravitationally bound objects, and the initial and the current cluster mass functions (e.g., Kumai et al. 1993; Elmegreen & Efremov 1997; Bastian et al. 2011).

The keystone of such studies relies on our ability to estimate stellar cluster intrinsic properties, in particular, their ages and masses. Much observational effort has therefore been invested to determine the distributions of star cluster ages and masses (Searle et al. 1980; Larsen & Richtler 2000; Billett et al. 2002; Hunter et al. 2003; Fall et al. 2005; Rafelski & Zaritsky 2005; Dowell et al. 2008; Larsen 2009; Chandar et al. 2010; Bastian et al. 2011), and to determine the dominant mechanisms of cluster formation and disruption (Kroupa & Boily 2002; Boutloukos & Lamers 2003; Lamers et al. 2005; Whitmore et al. 2007; Parmentier & de Grijs 2008; Fall et al. 2009; Elmegreen & Hunter 2010; Converse & Stahler 2011). However, most of the literature deals with observations of relatively massive clusters (a few $10^4 - 10^5 M_{\odot}$), therefore, quite insensitive or stable in various environments. Only a few studies have been able to probe smaller clusters (mainly in the Galaxy or the Magellanic Clouds).

The Panchromatic Hubble Andromeda Treasury (PHAT; Dalcanton et al. 2012) is an ongoing multi-cycle Hubble Space Telescope (HST) program. PHAT represents a gold-mine for the study of stellar clusters in M31. It aims to image one-third of the M31 disk at high spatial resolution with wavelength coverage from the ultraviolet through the near-infrared. The sensitivity of the latest HST instruments allow us to detect clusters in M31 down

to a regime in which cluster luminosities overlap those of individual bright stars, and hence to very low masses (Johnson et al. 2012). This survey spans a wide range of star-forming environments in both formation intensities and gas densities. This diversity is an advantage for addressing the relationships between cluster formation and evolution to their environment.

The PHAT survey has already significantly increased the number of clusters known in M31; it allowed the identification of 601 stellar clusters (Johnson et al. 2012) before reaching the first third of its coverage, representing more than a factor of four increase in the number of known clusters within the current survey area. Moreover, the simultaneous accessibility of a uniform photometric coverage from the UV to near-IR of the PHAT data provides an unprecedented quality sample of clusters available to study extragalactic clusters. As a result, accurate age-dating, as well as the ability to probe a broad range of stellar properties is now possible.

Finally, this preliminary sample offers a pioneer sample of clusters outside the Milky Way and the Magellanic Clouds, probing about 2 orders of magnitudes fainter in the luminosity function.

This paper is part of a series utilizing the PHAT dataset for studies of stellar clusters. Johnson et al. (2012), presented the first installment of a HST-based cluster catalog, which serves as the basis for an extensive study of Andromeda’s cluster population. In this paper, we focus on the determination of ages and masses of the currently available sample looking forward to the final product of this four year Treasury program. Our estimates of the properties of the clusters are derived from integrated photometry in 6 broad bands and we especially focus our attention on the characterization of the lowest-mass clusters. Additional studies, including analysis of structural parameters, resolved star content, and integrated spectroscopy of the cluster sample will follow in subsequent work.

This paper is organized as follows. §2 presents the cluster sample and the key elements of their photometry. §3 describes the analysis and the cluster models we used to derive the properties of the clusters, and we briefly highlight the possible artifacts of the method using synthetic data. §4 describes our results for the entire sample and for individual regions across M31. And finally we discuss those results in §5 before drawing our conclusions.

2. Observations & Cluster catalog

For this paper, we use 601 cluster candidates from the Johnson et al. (2012) Year 1 catalog, which contains integrated photometry through six broad-band filters from the UV to the near infrared: F275W (*UV*), F336W (*U*), F475W (*g*), F814W (*I*), F110W (*J*), F160W (*H*). Clusters were detected by-eye, primarily based on the F475W images, and visually classified based on their sizes, shapes, and concentrations as explained in Johnson et al. (2012).

The Year 1 catalog is sub-divided in regions called “bricks”, following the survey observation strategy. The cluster catalog includes four full bricks (designated B01, B09, B15, and B21; numbers increase with increasing galactocentric radius) as well as the western halves of two additional bricks (B17W and B23W). For simplicity, we group B17W with B15 and B23W with B21, respectively, for the remainder of this work, since both pairs form contiguous regions. These data sample locations along the major axis of M31 in its core and at $\sim 6, 10$ and 15 kpc from the center of the galaxy. With the exception of the bulge dominated brick, B01, the remaining ones are located on various star forming environments: star forming ring or spiral arms, with B15 sampling the highest star formation intensity (in the “10 kpc-ring”). The color image in Fig. 1 illustrates the positions of the clusters in the catalog in the different observed regions relative to the expected final coverage of the survey.

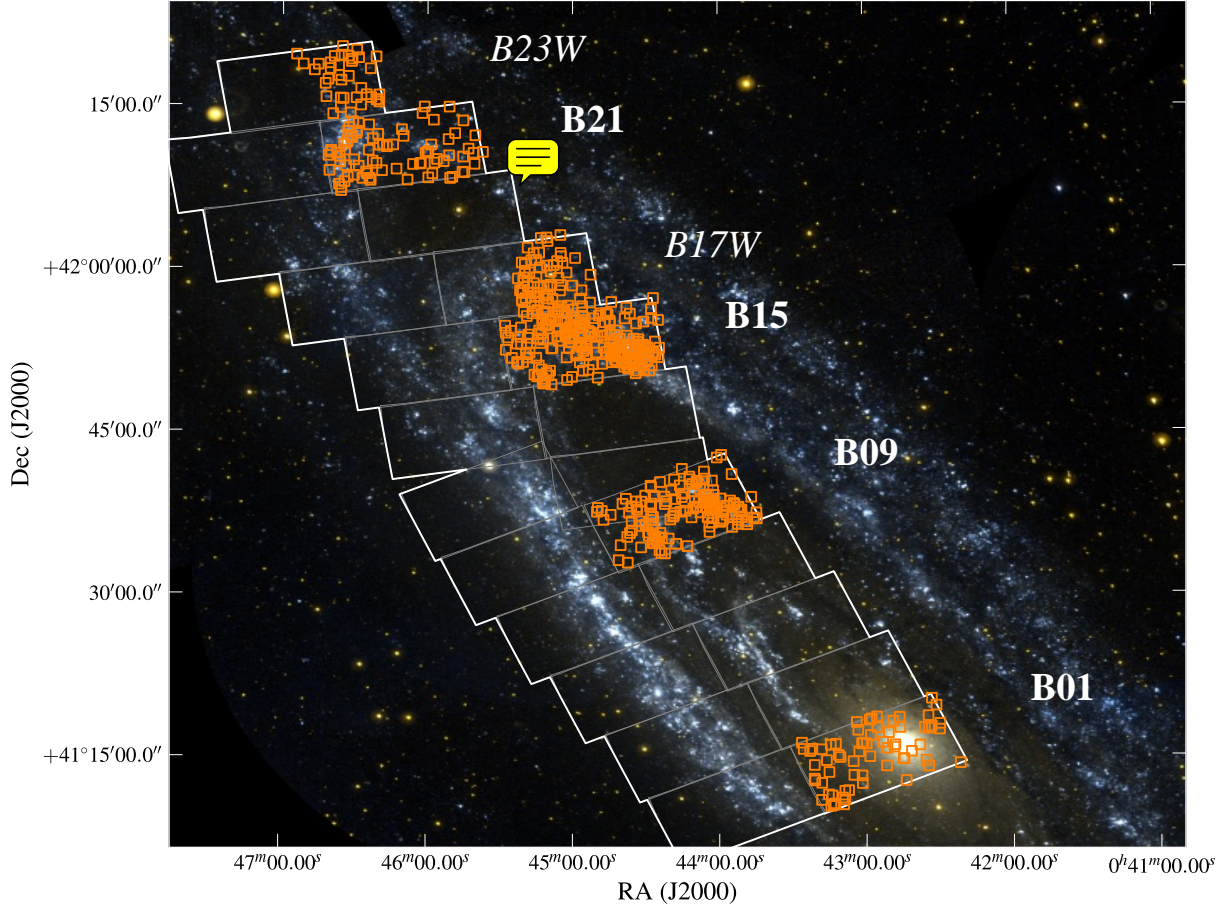


Fig. 1.— GALEX FUV-NUV composite image showing the positions of the clusters (orange squares) in the PHAT Year 1 Catalog. The white outer contour represents the footprint of the final survey, subdivided into rectangular “bricks”, shown in grey. Labels correspond to the names of the regions of interests mentioned in § 2.

We measured instrumental magnitudes for the clusters using aperture photometry. Measurements were converted into the VEGA magnitude system (see Johnson et al. 2012, §4.1.1 for details). We do not perform passband conversions and instead work with the native HST filters. We assume a distance of 785 kpc to M31 as found in McConnachie et al. (2005), which corresponds to a distance modulus of $m - M = 24.47$ magnitudes.

Assessing the completeness of cluster samples is a challenge on its own. The true completeness of the sample as a whole is indeed a complicated function of cluster luminosity, size, and location (strictly over three dimensions) within M31. The completeness of the sample was assessed by conducting artificial cluster tests. We used artificial clusters that span the range of values that we expected to find in the cluster sample. Specifically, we selected ages ranging from 4 million to 10 billion years and masses ranging from 10^2 to $10^5 M_{\odot}$. Although we will not exploit the information in the present study, cluster sizes were also included in the completeness determination with different half-light radii, assuming King (1962) profiles (see §3.1 of Johnson et al. 2012, especially their Fig. 6). On average, the 50% completeness limits in the F475W filter are $M_{F475W} = -3.8, -3.5, -2.8, -2.2$ for B01, B09, B15, and B21, respectively. Artificial clusters were also used to assess the uncertainties and biases associated with our photometry.

3. Deriving Cluster properties

In this section, we derive age-mass distribution of the clusters in M31, using the probabilistic method developed in Fouesneau & Lançon (2010). The method is particularly developed for the low-mass regime through a large collection of Monte-Carlo simulations of individual clusters. These simulations take full account of stochastic sampling of the stellar mass distribution, allowing robust Bayesian fitting to the observed colors of the observed clusters.

3.1. Population models

Synthetic clusters are constructed with the population synthesis code `Pégase.2n` (Fouesneau et al. in prep.), which is derived from `Pégase` (Fioc & Rocca-Volmerange 1997). As in the original population synthesis code, the underlying stellar evolution tracks are those of the Padova group (Bressan et al. 1993; Bertelli et al. 1994), with a simple extension through the thermally pulsating AGB based on the prescriptions of Groenewegen & de Jong (1993). The input stellar spectra are taken from the library of Lejeune et al. (1997). The stellar initial mass function (IMF) is taken from Kroupa et al. (1993), and extends from 0.1 to $120 M_{\odot}$. Nebular emission (lines and continuum) are computed as in Fioc & Rocca-Volmerange (1997) and are included in the calculated spectra and broad band fluxes under the assumption that no ionizing photons escape. The synthetic photometry for the artificial clusters is computed using the response curves of the PHAT HST/ACS and HST/WFC3 filters. A reference spectrum of Vega provides zero magnitude fluxes (Bohlin 2007).

The code uses Monte-Carlo (MC) methods to populate the stellar mass function (SMF) with a finite number of stars. As a result, it explicitly accounts for stochastic variations in the stellar content of populations. In the context of studying faint clusters in M31, the simulated cluster set has been extended to lower masses than available in Fouesneau et al. (2012), and now covers masses from ~ 50 to $5 \times 10^5 M_{\odot}$, and ages from 1 Myr to 20 Gyr. With a few $\times 10^8$ individual objects, the collection is large enough to include all reasonably likely cluster properties in this mass range. We also include a transition to continuous models above $4 \times 10^5 M_{\odot}$, motivated by the presence of about ~ 30 massive globular clusters in the PHAT catalog ($> 10^5 M_{\odot}$, Caldwell et al. 2011). For computational reasons developed in Fouesneau et al. (2012), the mass distribution in the collection of models follows a power law of index -1 . The ages of the synthetic clusters are drawn from

a power law distribution with index -1 (equal numbers per logarithmic bin), rounded to integer multiples of 10^6 yr. The extinction, A_V , is allowed to vary uniformly from 0 to 3 magnitudes with a fixed R_V of 3.1, with respect to the standard law of Cardelli et al. (1989).

For this first study, the metallicity, Z , is fixed to 0.02 (solar) for the discrete part of the collection and allowed to vary for the continuous massive clusters uniformly between the fixed values of $[0.004, 0.008, 0.02, 0.05]$, corresponding approximately to Small and Large Magellanic Clouds, Solar, and super-Solar metallicities, respectively. Based on HII region abundances, we expect young clusters to be well-approximated by solar metallicity, while globulars are known to have lower metallicities (e.g Zurita & Bresolin 2012; Caldwell et al. 2011; Cezario et al. 2012) For reference and regardless of the validity of the continuous assumption in the low-mass regime, we also provide the estimates derived from an analog probabilistic analysis based on continuous models only, extended over the same mass range. Individual cluster estimates are collected into Table B in Appendix B.

3.2. Analysis Method

The probabilistic method developed in Fouesneau & Lançon (2010) provides posterior probability distributions in the age-mass-extinction space (marginalized over the metallicity dimension), using multi-wavelength photometric observations and the above large collection of Monte-Carlo simulations of clusters of finite stellar masses. As in all Bayesian inference approaches, the results are stated in probabilistic terms, and they depend on *a priori* probability distributions of some model parameters (priors). In our context, the probability for one cluster to have a specific age, mass, extinction, and metallicity, given a set of photometric observations is:

$$\mathcal{P}(\theta \mid data) \propto \mathcal{P}(data \mid \theta) \times \mathcal{P}(\theta), \quad (1)$$

where the *data* are the 6 band photometric values, θ is the ensemble of parameter values (*i.e.*, age-mass-extinction-metallicity), $\mathcal{P}(\theta)$ are the “priors”, and $\mathcal{P}(\text{data} \mid \theta)$ is the likelihood of measuring an energy distribution for a given set of θ . We consider the same “normal”-likelihood function as used in Fouesneau & Lançon (2010) assuming the photometric errors are Gaussian.

The posterior probability distribution, $\mathcal{P}(\theta \mid \text{data})$, depends on the assumed age and mass distributions of the synthetic clusters, together with the values allowed for extinction. As described in § , our priors can be explicitly expressed as an independent combination of age, mass and extinction functions:

$$\mathcal{P}(\theta) \propto \text{mass}^{-1} \times \text{age}^{-1} \times K_{A_V}, \quad (2)$$

in other words, independent power-laws in age and mass, and uniform in A_V , respectively. The completeness limits of the observations are not used in any manner during the determination of individual ages and masses. The power-law distributions we have adopted mimic two major qualitative trends seen in star-forming galaxies: low mass clusters are more numerous than high mass clusters, and, because of a variety of efficient disruption mechanisms, young clusters are more numerous than old ones.

We characterize the quality of the fits of each cluster by assessing the probability of a “bad fit”, \mathcal{P}_{bad} . We define \mathcal{P}_{bad} as follow:

$$\mathcal{P}_{\text{bad}} = \left\{ 1 + \int \mathcal{P}(\theta \mid \text{data}) d\theta \right\}^{-1} \quad (3)$$

We can interpret this quantity as comparison of the likelihood of a spectral distribution with itself, to the likelihood of the spectral distribution with the predictions from the ensemble of models. In other words, \mathcal{P}_{bad} is the odds that none of the models can fit the data: it will tend to 1 when none of the models are able to describe the data, and it will tend to 0 if all the models are “perfect” matches.

Appendix B gives a table of individual values for each cluster of the sample, with both the discrete models (incl. continuous extension at the higher mass end) and continuous ones. When referring to individual property values, the quoted values are the age-mass-extinction triplets that maximize the posterior probability, i.e., maximize the probability of the observed set of fluxes, given the underlying priors. Quoted uncertainties are the projected percentiles ranges onto each individual parameters of the posterior.

Through samples of synthetic clusters, we characterized the potential artifacts and biases in the determination of cluster ages, masses and extinctions. Briefly, we generate 6-filter photometry for a sample of synthetic clusters, then perturb the measured magnitudes according uncertainties distributed as in the actual PHAT cluster data. We then re-derive the properties for these perturbed clusters, and compare the recovered values to those that were input. For different realizations, large errors in age occur for a few percent of the synthetic clusters, mostly at ages of one or a few Gyr due to the age-extinction degeneracy strengthens by the addition of the metallicity as a new parameter. However a visual inspection of the color-magnitude diagrams (CMDs) of such clusters will detect catastrophic errors. As a result, we visually inspected the CMDs of each observed cluster and added a caution flag in Table B when we estimate a failure of the fit, this represents 60 clusters, mainly in the bulge. In further studies, we will update the models of clusters such that the metallicity will be a parameter of the fit. We will also include independent determination of the extinction and/or metallicity when available, which corresponds to a better set of initial priors Overall, we do not recover potential biases from the analysis of synthetic data. The dispersions we obtain are ~ 0.14 dex in mass and ~ 0.18 dex in age. Therefore, we will not venture to interpret features smaller than 0.2 dex in either age or mass space (conservatively, since the test dataset corresponds to perfectly modeled data). To reflect these limitations, we bin the posterior probability distributions to 0.2 dex in the subsequent figures.

4. Year 1 PHAT Clusters properties

The current PHAT cluster catalog is derived from the first third of the survey, and focuses on the bulge and three major star forming regions. In this section, we thus look at the first glimpse of what can be expected from the full balance of the PHAT stellar cluster survey.

4.1. Global picture

In Figure 2, we compare the *loci* of the observations with the reddening free discrete models, in four projections of color-magnitude space. The data are shown together with 1% of the complete set of models, which will be used to assign age, mass and extinction estimates to each individual cluster. Even though models plotted on this figure do not include reddening, the majority of the observed clusters lies well within the regions covered by the synthetic clusters. In contrast, *continuous* population synthesis models (shown by solid lines) are unable to reproduce some of the observations. For example, the top left panel of Fig. 2 show a significant fraction of the observations lying on the left side of the *continuous* age sequence, i.e. the solid line. Allowing for extinction will not help the *continuous* models to predict such colors. These colors correspond to relatively low-mass clusters (< a few $10^4 M_{\odot}$) without any post-main sequence star. However, there are also observations even bluer in the F475W–F814W color, lying outside both models range of predicted colors and fluxes. These observed cluster colors are particularly visible in the top left panel of Fig. 2. These clusters have large photometric uncertainties (not shown for figure clarity.). These “outliers” could potentially lead to bad quality estimates during the analysis. Recall we introduced \mathcal{P}_{bad} (Eq. 3) to characterize the quality of the results relatively to the models.

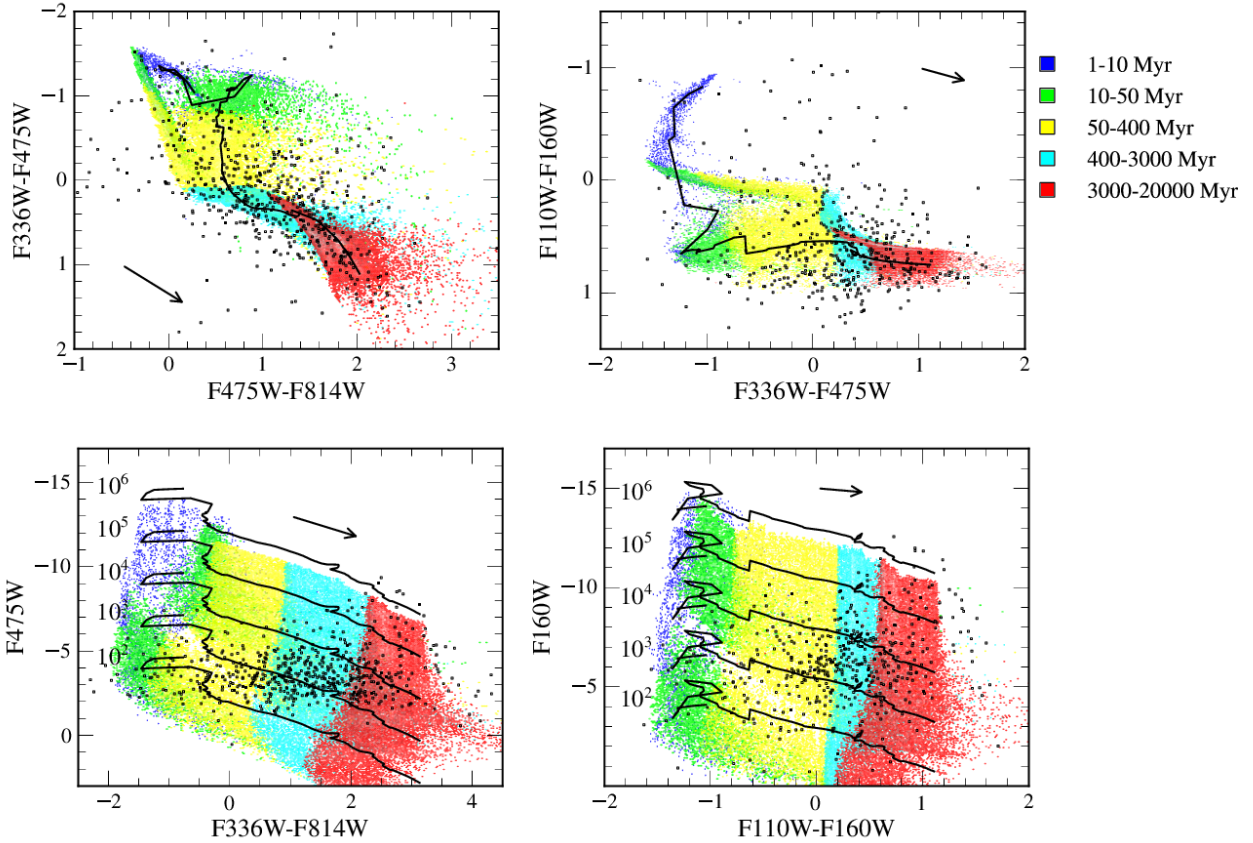


Fig. 2.— Color-color (top row) and color-magnitude (bottom row) ~~diagrams of the observed clusters (black points) and the models (color coded by age). Solid lines show the predictions obtained with the corresponding “continuous” population synthesis models for 10^2 , 10^3 , 10^4 , 10^5 , and $10^6 M_{\odot}$. Colored dots represent 1% of the discrete clusters available in the Monte-Carlo collection. The color code is given on the right hand side of the figure. Models are not reddened in any panel, but the extinction vector of $A_V = 1$ is shown for reference.~~ Magnitudes are in the Vega system, in the PHAT ACS and WFC3 filters.

The locations of the clusters in color and magnitude space draw the unsurprising picture of a cluster population spanning a wide range of age and mass. The entire length of the age sequence seems to be populated and the mass range suggests the presence of a significant number of clusters with masses well below $10^3 M_{\odot}$. The two bottom panels reveal a general trend that the most luminous clusters in this sample have old ages; these very old clusters fall above the $10^5 M_{\odot}$ curve, and are very likely to be old globular clusters. The typical completeness limit of -3 in the F475W band can be seen as the lower limit to the data in the bottom left panel.

Figure 3 shows the age-mass-extinction distributions resulting from the analysis described in §3. Each panel represents the joint probability distribution of 2 of the variables, after marginalizing over the third. The derived masses range from a little above the low limit of our model catalog ($50 M_{\odot}$) to a bit more than $10^6 M_{\odot}$. Ages are distributed between a few Myr and about 10 Gyr, with the few massive candidates appearing only for ages older than 5 Gyr.

At old ages, we do not expect many highly reddened clusters to be present, since they should have drifted far from their birth sites. However, unreddened clusters would have faded below the detection limits of the sample unless they were very massive. Moreover, cluster disruption processes are also in favor of lowering the number of old clusters. Both arguments explain the lack of old, low-mass clusters especially visible on the top panel of Fig. 3.

At the high-mass end, the main difficulty is the low birthrates, resulting in poor statistics. Although a large galaxy like M31 may have formed a few dozens of clusters above $10^5 M_{\odot}$, they are intrinsically rare. Apart from the fact that massive clusters are inherently rare, the age-mass distribution suggests that M31 did not produce as many massive clusters recently as it did a Gyr ago. We discuss the decrease in the rate of massive

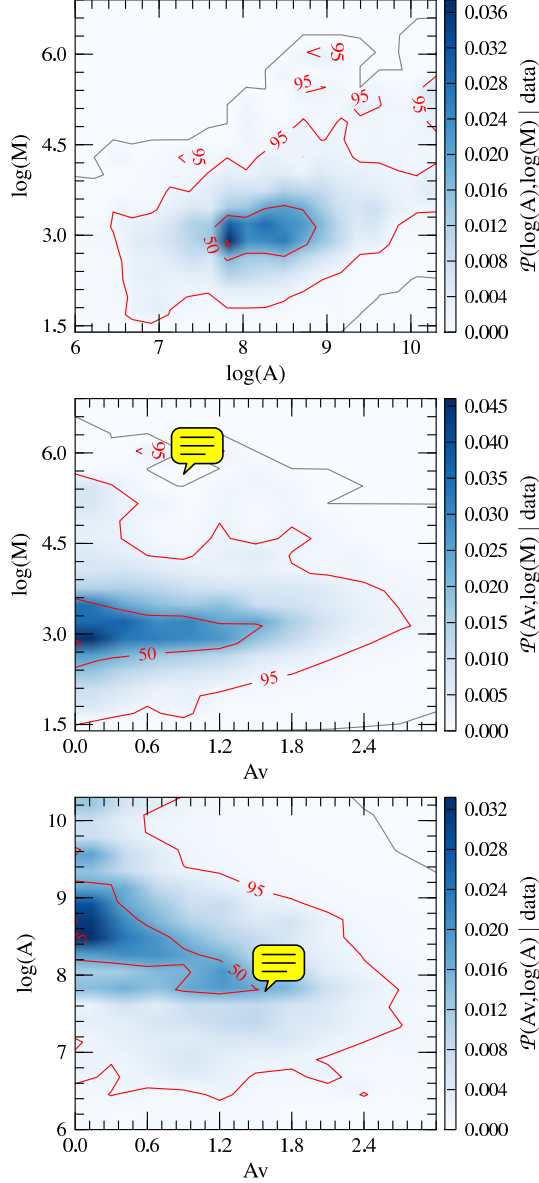


Fig. 3.— Joint probability distributions for age (“A”), mass (“M”) and extinction (“Av”) over the entire cluster sample. Each panel represents a distribution marginalized over the third parameter and color coded according to the scale on the right side of each panel. Red contours represent the 5%, 50% and 95% quantiles of the distributions in their respective 2D-space. The gray contour represents 99.9% of the joint distribution.

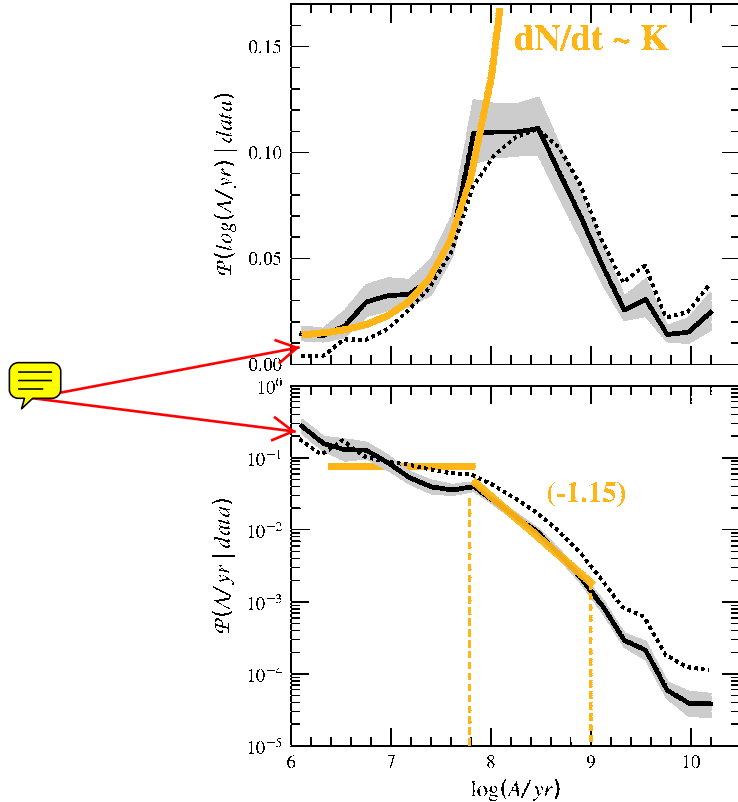


Fig. 4.— Age  marginalized distribution of the entire sample regardless of the positions of the clusters. Thick lines represent the total distribution while shaded regions are their respective uncertainties based on bootstrapping the cluster sample as described in the text (§4.2). The orange line on the top panel represents a constant cluster formation, over the last 100 Myr. It corresponds to the horizontal line on the bottom panel. To the latter, we have also added the best fit described in §4.2. Also shown of both panels, a dotted line corresponds to the age distribution restricted to masses above $10^3 M_\odot$, where effects of observational completeness are limited.

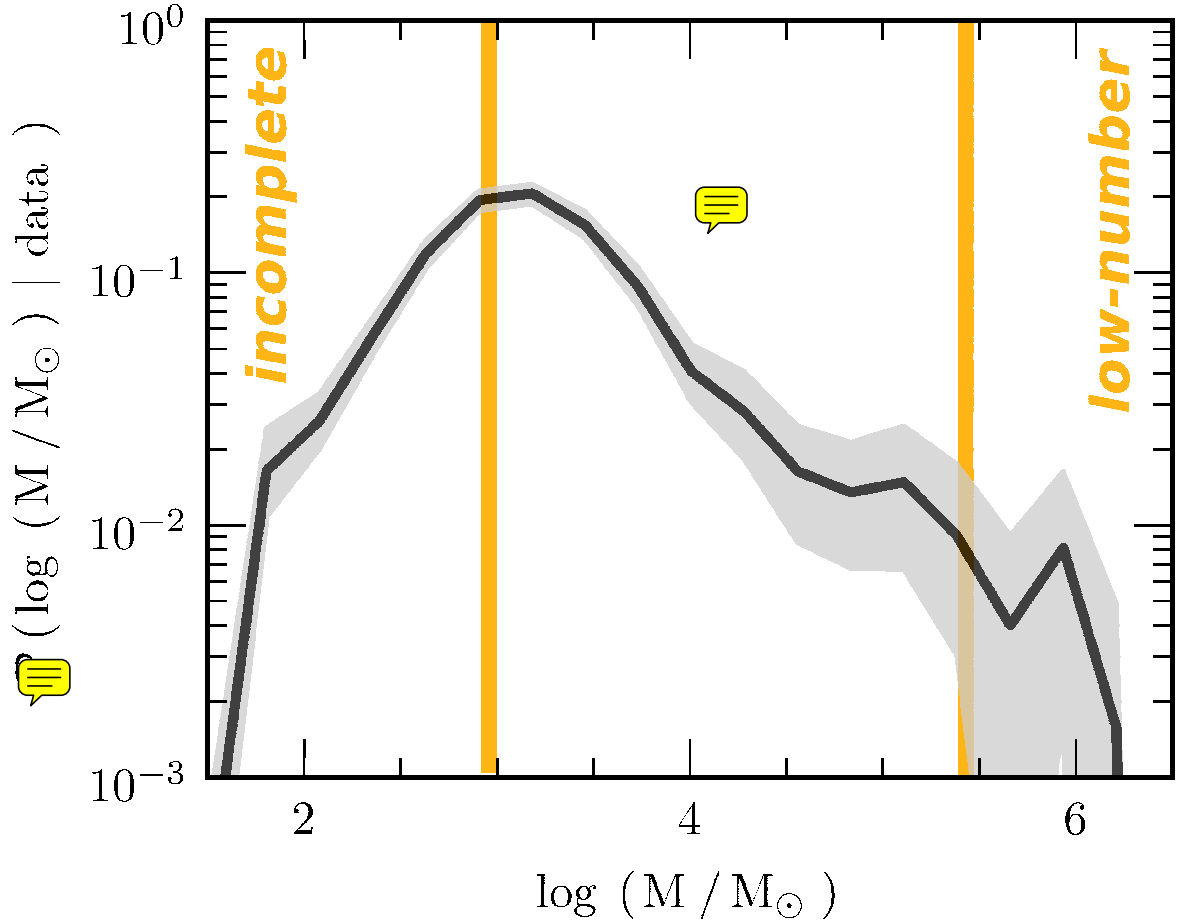


Fig. 5.— Mass marginalized distribution of the entire sample regardless of the positions of the clusters. Thick lines the total distribution while shaded regions are their respective uncertainties based of bootstrapping the cluster sample as described in the text (§4.2). The two vertical lines represent the regime limits where the distribution is less than 50%-complete (left) and stochastic presence of clusters in our sample is dominant: uncertainties are more than 50% of the value (right).

cluster production in more details in §4.2.

The bottom panel of Fig. 3 shows that very young clusters (although not in majority) come with a large range of extinction values, as has been seen in many star forming galaxies (e.g., Whitmore & Zhang 2002; Kim et al. 2012). At ages older than 10^8 yr however, clusters with more than one magnitude of extinction become rare. Between 10^7 and 10^8 yr, the absence of reddened clusters most likely reflects a real lack of highly reddened objects, rather than selection effects, given that the detection limits of the data would allow us to detect 5×10^7 yr old clusters with masses above $\log(M/M_\odot) \approx 4$. with up to more than 2 magnitudes of extinction.

4.2. Age distribution of the clusters

The age probability distribution represents the expected fraction of clusters at a given age (with respect to the cluster sample). In other words, this probability distribution represents the apparent age distribution of the clusters resulting from an underlying formation history (incl. stellar evolution and cluster disruption) combined with observational selections. The distinction of the age distribution from the cluster formation rate is analog to the differences between present day and initial mass function.

We can derive the age distribution of the ensemble cluster population by co-adding the age probability distribution functions (PDFs) of each individual cluster. This procedure produces a more accurate global age distribution than only assigning each cluster to its “best-fit” age, especially accounting for complex uncertainties. Moreover, probability distributions are more robust to binning effects, mainly because binning is applied to the collection of models ($> 10^8$ synthetic clusters).

The composite distribution of ages for the ensemble of clusters is shown in Fig. 4 (black

solid line). This figure shows two representations of the age distribution of the ensemble of clusters as function of logarithmic age. The top panel shows the probability distribution in $\log(\text{age})$ in contrast with the bottom panel showing the distribution of age . In both representations we also include dotted lines showing the composite distributions when restricted to masses above 10^3 M_\odot , the estimated completeness limit of our sample.

The uncertainties in the age distribution (represented by the shaded region on Fig. 4) are dominated by the random sampling of a finite relatively small (~ 600) sample of clusters. If we include or remove a very old cluster, e.g. 5 Gyr, the induced variations will be important because of low number of clusters at this age. In contrast, such alteration of the sample at 100 Myr will have less influence. In order to estimate sampling uncertainties, we characterize the variations of the posterior distributions by bootstrapping (Efron 1987; Rubin 1981). Specifically, we make 1000 realizations of the cluster sample, drawing randomly 601 clusters for each but allowing duplications. We re-derive the ensemble age distribution for each realization. The shaded region indicates the range containing 95% of the realizations of the age posterior distribution. Each individual realization is also used to further assess comparison uncertainties with different cluster age distribution models.

The age distribution (Fig. 4) shows that clusters span ages from a few Myr up to 10 Gyr. The young cluster age distribution is quite consistent with a constant over the last 100 Myr, indicated by the thick orange line on Fig. 4. The distribution drops off at ages older than 10^9 yr, as expected from cluster disruptions and the observational selection limits (as described in §4.1).

We fit a power-law with spectral index β to the observed age distribution of the whole sample over $\log(A/\text{yr})$ between 8 (100 Myr) and 9.0, using a χ^2 likelihood statistics:

$$\mathcal{P}(A/\text{yr}) \propto A^\beta, \quad (4)$$

We find that the age distribution of the sample can be approximated with a power-law

of index $\beta = -1.15 \pm 0.1$ over $\log(A/yr)$ between 8 (100 Myr) and 9.0. However, note that this power-law does not map directly into the cluster formation rate since no cuts have been applied to ensure that the same range of cluster masses is detectable at all ages. This old regime is consistent with the literature (e.g., Elmegreen & Efremov 1997; Hunter et al. 2003; de Grijs & Anders 2006; Chandar et al. 2010; Bastian et al. 2011; Fouesneau et al. 2012), which also find power-law age distributions with spectral indexes close to -1 . When we apply a mass cut at $10^3 M_\odot$, our expected mass completeness limit, the resulting cluster age distribution (dotted line in Fig. 4) does not significantly differ on the same age range from the previous result. On the contrary, this cut shows a better agreement with a constant rate at younger ages, especially visible on the bottom panel of Fig. 4).

In §4.4, we show that this age distribution is relatively the same for the individual regions covered by the current survey catalog.

4.3. Mass distribution of the clusters

The marginal distribution of all the cluster masses of the sample (i.e., the distribution summed over all ages and extinctions) is shown in Fig. 5. We derived the composite distribution of the whole cluster sample from their individual probability distributions as described for ages in §4.3. However we caution against extracting information from: (i) the low-mass regime, where below $\sim 10^3 M_\odot$ the sample is less than 50%-complete; (ii) the upper-mass regime, where the rare presence of one single massive cluster can induce large variations in the distribution. This stochastic sampling of the cluster mass function can result in large fluctuations of the upper-mass end. As a result, we conservatively define a mass upper limit as the mass where the uncertainties are more than 50% of the median value, where the errors are obtained from bootstrap re-sampling (*c.f.* §4.2). These two regimes are delimited by the vertical thick lines in Fig. 5.

Over the interval of $10^3 - 10^{5.5} M_\odot$, the distribution of masses for the entire sample can be approximated by a power-law,

$$P(M/M_\odot) \propto M^\alpha, \quad (5)$$

with index $\alpha = -1.73 \pm 0.11$. The age distribution of clusters, as presented in § 4.2, presents a significant change in its shape pasted a 100 Myr. When we restrict the sample to only clusters with ages between $10^7 - 10^9$ yr, the distribution becomes steeper with an index of -1.89 ± 0.12 , over the same mass range. However this remains statistically compatible with the fit of the full distribution. We do not extend the fit over 10^9 yr because the incompleteness of the sample may significantly impact conclusions from this regime. Overall, we find a power-law behavior of the cluster mass function, which agrees with previous analyses of other galaxies (e.g., in Fig. 10 of the review from Portegies Zwart et al. 2010). In particular we find a close match with a power-law with spectral index -2 in agreements with several cluster mass function determinations with indices close to 2 (e.g. Zhang & Fall 1999; McCrady & Graham 2007; Bik et al. 2003; Chandar et al. 2010).

The mass distribution has an apparent peak near $\log(M/M_\odot) = 3$, which falls off towards lower masses. Based on the Monte-Carlo collection, we know that $\log(M/M_\odot) = 3.1$ is the threshold mass under which more than half of the clusters have fluxes below the “50%-completeness” limit (defined in §2) in at least the F475W photometric passband. This peak is likely due to the incompleteness of the cluster sample at low fluxes, given that the model clusters are well populated down to much lower masses. The exact characterization of this peak is uncertain, because: (i) being faint, the low mass objects have larger observational errors than massive ones; (ii) clusters that have low masses while remaining above the detection limits must be young, and therefore we are in the regime most sensitive to the modeling; and (iii) the detection of such low mass clusters becomes very difficult by eye, since their contrast with the field becomes very unclear.

4.4. Galactocentric variations

In this section we explore potential variations in the distributions of cluster properties across the galaxy.

Figure 6 shows the 2-D joint parameter distributions for each of the bricks, equivalent to Figure 3, but subdivided by regions. Figure 6 highlights the variable completeness of our sample across the galaxy: indeed, it is very difficult to detect low-mass and/or highly extinguished clusters in the bulge, because of the high luminosity background. In contrast, it becomes very easy to find them in the outer part of the disk. From the four top panels of Fig. 6, one can see that the effective 95% completeness moves ~ 1 dex in both age and mass, such that older and lower-mass objects are more detectable at increasing radius. This effect is reflected by the translation to the left of the diagonal limit in the bottom right corner of those panels.

Figure 6 shows that the difference between the bulge and the other regions is very strong; we observe that most of the massive old clusters are in the bulge. This corresponds to the bulk of the globular clusters from our sample. In contrast, we find the lowest-mass clusters mainly in the outer regions of M31 (B15 and B21), which have the lowest stellar density, and thus the best contrast for detecting low-luminosity clusters. Moreover, all of the disk fields are quite similar, beyond the small variations in sensitivity. As a result, for the rest of this paper will consider only the disk fields (B09, B15, and B21).

Figure 7 compares the marginalized age and mass distributions for each of the three outer regions, following the same conventions as Figs. 4 and 5. The black line reproduces the distribution of the whole sample. There are roughly twice as many clusters in B15 relative to the two other regions, and therefore larger uncertainties are associated with the distributions in the inner (B09) and outer (B21) regions, compared to those for clusters in the 10 kpc ring (B15)

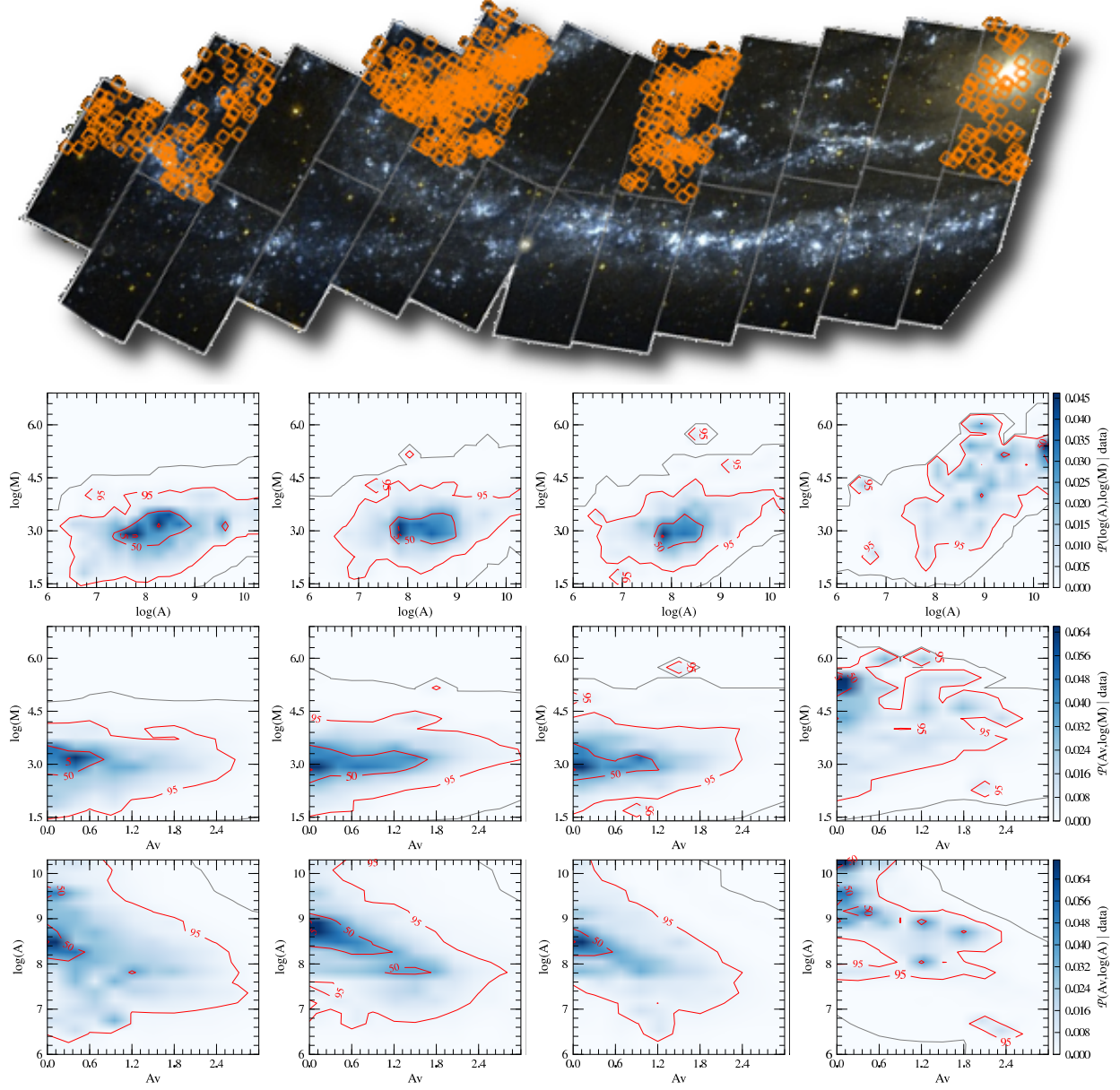


Fig. 6.— Joint 2-D probability distributions (Bottom 3 rows) for age (“A”), mass (“M”), and extinction (“ A_V ”), for 4 different sub-regions of M31 (shown on top row, with 4 clumps of cluster positions at B21+, B15+, B09 and B01, left to right columns, respectively). This figure is an analogous of Fig. 3, which shows the equivalent distributions for the entire sample.

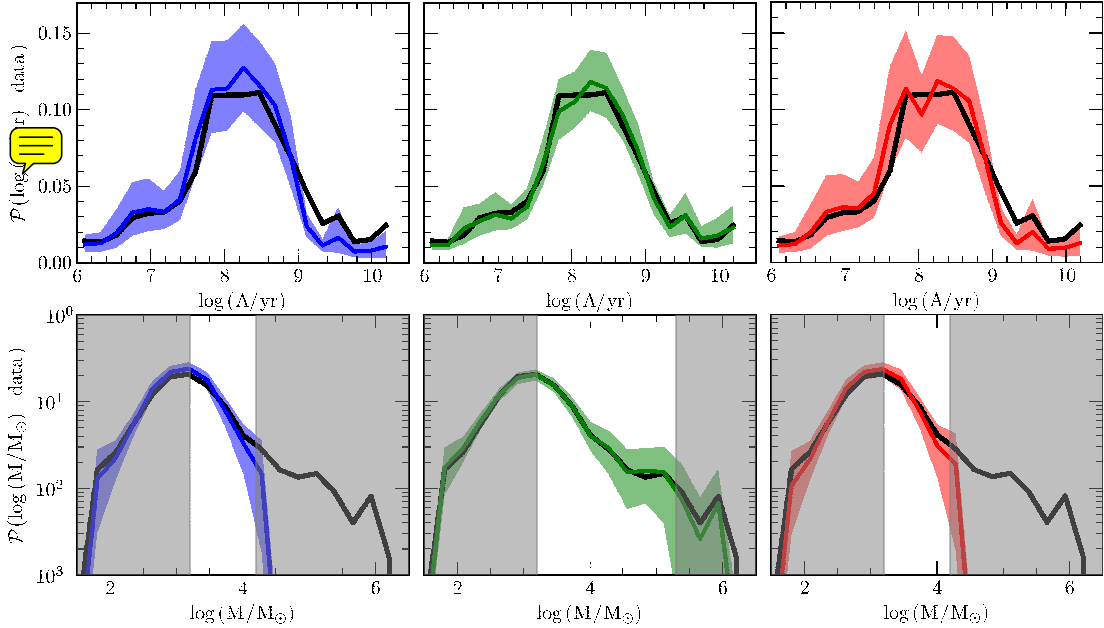


Fig. 7.— The individual marginalized probability distributions for age (top row) and mass (bottom row), for clusters in Bricks 9, 15+, and 21+ (left to right, respectively). Each column represents the distributions derived within a single brick. Shaded colored regions indicate the uncertainties in the distributions, derived from bootstrap re-sampling. For reference, the black lines show the distribution derived for the entire sample (e.g., Figs. 4 & 5). Gray shaded regions on the mass plots indicate regions where either completeness or stochastic sampling of the massive clusters are dominating the distributions. These regions are not included when fitting the distributions with power-laws.

Age distributions The top panel of Figure 7 shows that there are no significant changes in the local age distributions, as we move radially away from the center of the galaxy. Figure 8 facilitates the cluster formation rate comparison between the different bricks. At young ages (< 100 Myr), all age distributions of cluster sub-samples are consistent with a constant formation over the last 100 Myr, suggesting that any variations in the cluster formation rate were coherent over the galaxy. At older ages (> 100 Myr), the age distributions in B09, B15, and B21 are all compatible with a power-law. The power-law spectral indices for each age distribution in Fig. 7 are -1.39 ± 0.1 , -1.11 ± 0.1 , and -1.21 ± 0.1 , for brick 9, 15, and 21, respectively. As a reference, in §4.2 we found that the overall sample could be approximated with a power-law of index -1.15 ± 0.1 over $\log(A/\text{yr})$ between 8 (100 Myr) and 9.0. The broad similarity among the age distributions (illustrated in Figure 8 by the orange shaded region) suggests a common cluster formation history within the three different forming regions. In other words, changes in the cluster formation rate were coherent across the galaxy. In contrast, the cluster sample spans a broad range of environments. In particular, we expect variations in the local gas density, which should lead to different cluster disruption efficiencies (Boutloukos & Lamers 2003; Lamers et al. 2005). However we do not observe statistically significant differences in the age distributions of clusters from the ring (B15) and the most outer-region (B21), where the gas density is the highest and the lowest, respectively.

Unfortunately, the current data are not sufficient to distinguish statistically significant variations from brick to brick. While it appears to be a radial variation in the position of the roll-over of the distribution, a reliable interpretation of the roll-over is difficult without larger samples and a better characterization of the completeness effects. We have postponed this analysis to our analysis of the full PHAT dataset.

Mass distributions The bottom panels of Fig. 7 present the mass distributions of all of the clusters in the 3 disk fields. The shaded regions follow the same conventions as in Fig. 5. The lower-mass regime is defined to be the region where the sample is less than 50% complete. We strictly define this limit conservatively at $\log(M) = 3.2$ such that we can assume the same value in each region. The upper limit is set where the uncertainties are more than 50% of the median value (as explained in §4.3). The upper mass limit is very different in the ring (B15) due to the presence of more massive clusters than in the two other regions (B09 and B21) although the latter two are similar. This expectation is due to the factor of 2 to 3 variation in the number of clusters per brick. For stochastic sampling of a power-law distribution, the number of massive clusters in each region is expected to vary significantly (a factor of 10, see Table 1). We discuss the lack of massive clusters in §5.3.

Qualitatively, B09 and B21 share a similar mass distribution, whereas the mass distribution in B15 appears to be different. To quantify the differences, we have fitted the distributions with a power-law for each region, similarly to §4.3, while accounting for their associated uncertainties. Fig. 9 shows the resulting mass spectral index probability distributions. We obtain broad distributions for α for B09 and B21, as expected from the limited mass range used during the fit. We find a relatively narrow distribution for B15. Although all of the three distributions of α are compatible with a power-law of index of -1.8 found in §4.3, the differences from this overall description are significant (values and standard deviations: B09: -2.2 ± 0.17 , B15: -1.8 ± 0.1 , and B21: -2.1 ± 0.14). The variation favors shallow mass function where the stellar formation is the most intense and the gas content is the most important.

Brick	R_{gal}	F475W _{lim}	N_{cl}	N_{cl}	best	best	M_{max}
Name	in kpc	at 50%		$M > 10^3 \text{ M}_\odot$	β	α	M_\odot
		(1)			(2)	(3)	(4)
B01	0	-3.8	61	61	—	—	—
B09	6	-3.5	138	70	-1.11 ± 0.1	-2.2 ± 0.17	2.5×10^4
B15	10	-2.8	281	165	-1.21 ± 0.1	-1.8 ± 0.1	1.7×10^5
B21	15	-2.2	116	54	-1.39 ± 0.1	-2.1 ± 0.14	2.0×10^4

(1) 50% Completeness limit in F475W (Johnson et al. 2012),

(2) best age spectral index: $P(A/\text{yr}) \propto A^{-\beta}$ (§4.4),

(3) best mass spectral index $P(M/\text{M}_\odot) \propto M^{-\alpha}$ (§4.4),

(4) maximum expected mass from a power-law with index given by their best β (§5.1).

Table 1: This table summarizes the properties of each “brick” we obtain in this study. M_{max} is the expected upper masses in each brick assuming a fully populated cluster mass power-law of index -2 above 10^3 M_\odot and a constant cluster formation rate.

5. Discussion

5.1. Exploration of possible systematics

We have compared the cluster populations in 3 star forming regions in M31, and may have identified the first significant variation of the cluster mass function of clusters within one galaxy. On the other hand we find similar age distributions. We now explore the possible observational artifacts affecting our analysis.

Systematics from the analysis method We have made multiple assumptions when deriving ages and masses for the cluster samples. Some could lead to systematic errors in the masses.

First, we assumed in the models that no ionizing photons escape from the cluster. If some photons do escape, then we will over-estimate the flux in the nebular emission (continuum + lines), thus the model colors will vary. These color variations will shift clusters to different apparent ages, but slightly different masses. In contrary we find very similar age distributions, and significant variations in the observed mass functions.

Second, there may be some level of inconsistency between the stellar evolution models and the actual clusters. However, such an effect would be apparent in all regions, and would not produce radial variations.

Third, the lower-mass limit of the current collection is sufficiently low that the choice of the stellar IMF can affect the derived SEDs. If real clusters have a different mass function than we assumed, then the cluster ages and masses would be biased. Again this would not produce a radial variation in the mass distribution of the clusters without need to invoke an environmentally dependent stellar IMF.

Finally, our choice of priors during the analysis of cluster colors may not be optimal:

we assumed uniform expectation in age and mass on logarithmic scales. Since a variation of the prior assumptions does not significantly affect the resulting distribution of the sample as a whole, this is again not likely to produce variations in the cluster mass distribution across the galaxy (unless we consider variable priors according to environmental conditions).

In general, none of the above possibilities appears likely to produce the observed radial variations in the cluster mass function while keeping similar age distributions. Instead, mass estimates are known to be the most stable estimate in SED fitting of star clusters (e.g. Maíz Apellániz 2009; Fouesneau & Lançon 2010). Furthermore, all seem likely to affect all of the regions in a similar manner (outside of the bulge).

Selection effects in the cluster sample Our analysis is based on the cluster sample from the Johnson et al. (2012) catalog. Like any catalog, the resulting sample has biases that reflect how the clusters were selected. Johnson et al. (2012) adopted a definition of a “star cluster” to be a group of stars assumed to form a coeval population (i.e., single age, metallicity, etc.). This definition includes any clustered stars regardless of whether they are gravitationally bound or not. It is therefore possible that the observed variations are due to changes in the relative numbers of gravitationally bound clusters and unbound associations. Associations are most likely young because of their intrinsic instability. When their size is comparable to stellar clusters, they are also likely to be relatively low mass. In contrast, massive or dense groups of stars generate a potential deep enough that they are eventually bound.

However we do not observe a significant change at young ages between the three different regions. Including many low-mass objects could result in a steeper mass function. The outer most region (B21) is especially ideal for finding faint objects because of its low background and relatively low density of sources and extinction in comparison to other

regions. Hence, if this is a source of contamination, B21 should be the most affected. However, as shown in §4.4, B21 is similar to B09, which is the inner most region used in this comparison.

Completeness variations and missing low-mass clusters The completeness is in fact (i) a complex function of 6 filters photometry affected by measurement errors, (ii) does not translate into a single mass cut in the age-mass plane. Moreover, clusters in this sample are partially resolved into stars, which increases the complexity of a completeness estimation. From the observational limits given in Johnson et al. (2012), we derived an approximative mass completeness of $\sim 10^3 M_{\odot}$ using our collection of synthetic models.

We applied a conservative mass cut during the determination of the spectral index of the mass functions in order to reduce potential biases (e.g. Weisz et al., *submitted*). However Brick 15 is the most gas rich of the 3 forming regions, which could significantly increase the level of incompleteness in this region.

We can estimate the number of “missing” clusters in Brick 15 by comparing both power-law with index -1.8 (as the median value in Brick 15) and -2 . It requires a factor of ~ 5 more clusters between 10^3 and $10^5 M_{\odot}$ to recover a spectral index of -2 . This corresponds to 20 missing clusters above $10^4 M_{\odot}$, i.e. with more than 2 magnitudes of extinction. Although it is likely to induce variations in the age distribution as well, we cannot exclude this possibility without a more stringent assessment of observational completeness.

5.2. Age distribution and the cluster formation history

In this study, we find that the clusters age distribution, dN/dt (bottom panel of Fig. 4, is globally flat over the last 100 Myr. There are other cluster samples from the literature presenting the same constant distribution at young age (e.g., Lamers et al. 2005 limited to 600pc from the Solar neighbourhood; in the SMC flat over 1 Gyr by Hodge 1987; Chiosi et al. 2006). More over, we find a drop-off at older ages consistent with a power-law behavior of index -1.15 in agreement with the literature. Note that the catalog from Johnson et al. (2012) is highly biased towards the star forming regions of M31. Hence the derived typical values may vary when we eventually include the complete sample from the PHAT survey.

However, the interpretation of the dN/dt distributions is heavily dependent on how incompleteness of the sample of cluster is treated. Our cluster sample contains 600 clusters, luminosity limited and covers different star forming environments.

In order to characterize the cluster formation history of M31, we need assumptions on the cluster formation rate and disruption efficiencies. Under the assumptions that a cluster population formed at a constant rate and with a *power-law initial cluster mass function* (ICMF) with index α , and *no dissolution*, Gieles & Bastian (2008) demonstrate the age distribution of all clusters can be analytically estimated. Based on continuous population synthesis flux predictions, they show that the age distribution should follow a power-law dN/dt distribution with an index of ~ 0.7 , if the sample is limited by one optical band detection, and dN/dt should be constant if the sample is mass limited.

We do find a uniform distribution over 100 Myr, followed by a power-law. The index of the latter appears steeper than the index induced by fading only. Although disruption is a source of variation, selection effect and especially the incompleteness can increase the steepness of the distribution.

If we assume that all the clusters are detected at young ages, i.e. a complete sample, then we should obtain a constant distribution until the age that the fading or disruption starts to remove clusters from the sample. Independently of the region of the galaxy, we do find that the drop-off occurs at ~ 100 Myr. If disruption affects the cluster evolution, the environmental dependency must be weak compared to incompleteness effects.

5.3. Truncated Mass Function

The mass range on which we fit the mass distribution with a power-law distribution varies from one region to another. This variation is motivated by the lack of massive clusters in B09 and B21 in contrast with B15. Other studies have found evidence for a truncation of this power-law at the high-mass end (e.g Bastian & Gieles 2008; Larsen 2009; Vansevičius et al. 2009, in M31 for the later).

If the total cluster formation rate and the cluster mass function are known, we can calculate how many clusters in a given mass range should have formed over some time interval. We can, in particular, estimate the most-massive cluster we would expect and compare to our observations.

If we consider a constant cluster formation and a cluster power-law mass distribution defined over the given mass range $[M_1, M_2]$,

$$\mathcal{P}(M / \text{M}_\odot) \propto M^\alpha, \quad (6)$$

with α the spectral index of the mass function, we can define the probability to obtain a cluster with a mass m above a given mass M as follow:

$$\mathcal{P}(m \geq M | \alpha) = \frac{\int_M^{M_2} x^\alpha dx}{\int_{M_1}^{M_2} x^\alpha dx}, \quad (7)$$

We need then to introduce the total number of clusters, N_{cl} , formed from the mass

distribution. If we consider independent draws from this mass distribution, then the expected maximum mass M_{max} is satisfies the condition that we have one and only one cluster for $m = M_{max}$, therefore:

$$1 = N_{cl} \times P(m = M_{max} | \alpha) \quad (8)$$

$$M_{max} = \left\{ M_2^{\alpha+1} - \frac{1}{N_{cl}} \times (M_2^{\alpha+1} - M_1^{\alpha+1}) \right\}^{-(\alpha+1)} \quad (9)$$

When considering the upper mass limit M_2 to be infinite (and $\alpha < -1$):

$$M_{max} = M_1 \times N_{cl}^{\alpha+1} \quad (10)$$

Figure 10 shows the different expected distributions of M_{max} for each field brick of our study. The different curves are constructed from Eq. 9, when the mass function is defined within $(10^3 - 10^7 M_\odot)$. The mass range is chosen to be within completeness limits. The number of clusters above $10^3 M_\odot$ for each region is taken from Table 1. In Section 4.4, we fit the mass distributions of the different field regions. The upper mass limit values were chosen at the point where the uncertainties on the mass distribution become more than 50% of the estimated value. The values are reported on Figure 10, indicated by the black crosses, for which the spectral indices correspond to the best values obtained in §4.4.

The comparison shows the lack of massive clusters in B09 and B21 is consistent with a stochastic sampling of a power-law mass distribution. The mass cut we applied to Brick 15 appears a factor of 2 under the theoretical sampling prediction of the cluster mass function. Only 3 – 4 clusters above $10^5 M_\odot$ are present in this region, which leads to large uncertainties at this regime. Overall, the mass cut we applied during the fit are conservative.

5.4. Mass distribution and relation to the environment

The cluster sample from Johnson et al. (2012) is mainly focused on 3 different star forming environments (and the bulge) of M31. First, we found 2 to 3 times more clusters in the region centered on the 10 kpc ring (B15), in which the star formation intensity is measured to be 3 to 5 times higher when compared to the two other field regions (Williams 2003). The cluster mass function in B15 appears shallower compared to B09 and B21.

We briefly discuss multiple physical processes of cluster formation and evolution which could affect the cluster mass function.

First, the “infant mortality” paradigm, in which the process of going from the embedded to the exposed phase is responsible for the destruction of clusters in their early ages (Lada & Lada 2003). However, because it is mainly an internal process, we expect the depletion of the gas in a cluster to be largely independent of the environment (e.g., Goodwin & Bastian 2006). Hence, infant mortality cannot be a source of variation in the cluster mass function across the galaxy.

Second, clusters are subject to internal processes (e.g., relaxation, stellar evolution) and external interaction with their galaxy host (e.g., tidal field). Theoretical and analytical approaches to describe those processes (e.g., Hénon 1961; Spitzer 1987; Gieles et al. 2011) find that the lifetime of a cluster depends on its environment and its mass. Empirical models exist to predict the disruption of clusters (see Larsen et al. 2008, for a thorough review). Two families are mainly advocated: a “Mass Independent Disruption” (Whitmore et al. 2007) scenario, in which cluster disruption is independent of cluster mass and the ambient environment, and clusters are destroyed through strong interactions with the interstellar medium (but strongly linked with the ambient density of the gas (Elmegreen & Hunter 2010; Kruijssen et al. 2011)), and, in contrast, a “Mass Dependent Disruption” (Boutloukos & Lamers 2003; Lamers et al. 2005) predicts that the lifetime of a cluster

depends on its initial mass and the tidal field local intensity.

However, it is very hard observationally to distinguish between the cluster disruption scenarios, and the role of the different actors (cluster mass, tidal field, gas density, etc.) during the process. There have been only two galaxy studies in which a comparison of the two scenario families was conducted: in the Small Magellanic Cloud (Chandar et al. 2006; Gieles et al. 2007) and in M83 (Bastian et al. 2011). In both studies, the observed variations of the present day cluster mass function (PDMF) are not as significant as what is found here. The Johnson et al. (2012) Year 1 catalog probes much lower mass ranges in comparison, a regime most likely sensitive to environmental dependencies.

A comparative study of the disruption scenarios will benefit from the various environments the PHAT cluster sample will eventually provide. A preliminary comparison goes beyond the scope of this paper and will be presented in further work.

6. Conclusions

We have analyzed the PHAT cluster sample from Johnson et al. (2012) by comparing the integrated 6-filter fluxes of the clusters with an extended version of the stochastically sampled model clusters presented in Fouesneau & Lançon (2010).

The locus of the collection of stochastic models in color space (e.g., Figure 2) shows excellent agreement with that of the collection of cluster observations. Clusters with broadband colors either bluer or redder than those of the traditional models find a natural match with the models we used in this paper.

We generated the full probability distribution function of the correlated age, mass, and extinction for each of the 601 individual clusters in the sample. We then combined their individual distributions into global cluster age and mass distributions, noting limits

at which completeness issues in the sample become severe.

We find that the cluster age distribution shows a constant number of clusters over the last ~ 100 Myr, with a power-law decline at older ages. Although M31 seemed to produce a constant number of clusters from 100 Myr ago to present, we note a lack of massive young clusters suggesting a decline in the fractional mass formed in cluster environments.

The mass distribution derived from the analysis closely resembles the power-law distributions obtained from many other galaxies. Specifically, the overall power-law index of the mass distribution is consistent with the canonical value of -2 . However, the current cluster sample suggests a possible radial variation of this distribution across the disk.

As we include lower masses and compile larger samples of fainter clusters, the improved accuracy and time resolution achievable with the new stochastic methods allows us to address new questions. Future work will account for the challenging determination of completeness and selection effects. In particular, the expected number of clusters in PHAT will eventually provide 3 times more clusters over a broad panel of local environments, which will open the possibility to study local variations among cluster populations.

The authors acknowledge the efforts of the entire PHAT collaboration in this project. This paper is based on observations taken with the NASA/ESA Hubble Space Telescope obtained at the Space Telescope Science Institute, which is operated by AURA, Inc., under NASA contract NAS5-26555. Support for this work was provided by NASA through grant number HST-GO-12055

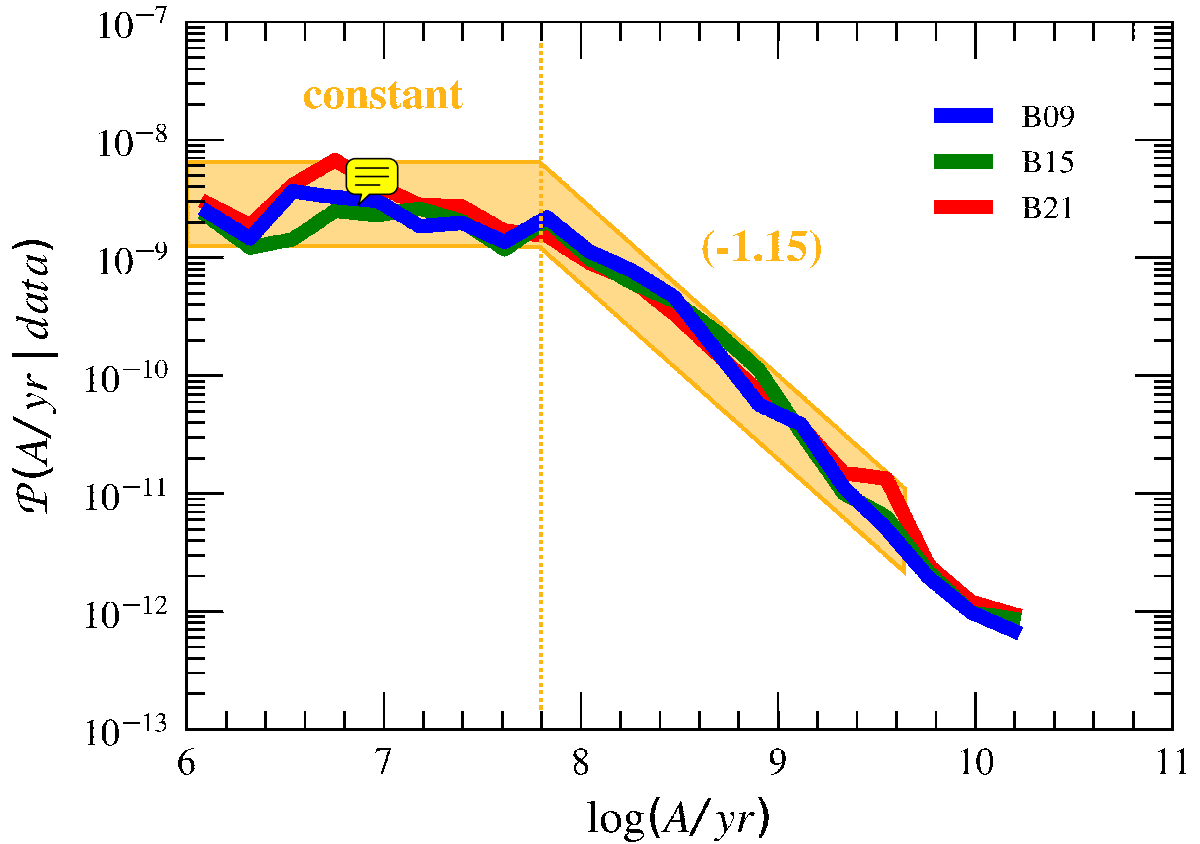


Fig. 8.— Distributions of cluster ages per linear age bins for each individual brick. This corresponds to the bottom panel of Fig. 4 for the clusters in each of the three regions in the disk. The orange shaded region illustrates the cluster age distribution described in §4.4: constant over 100 Myr followed by a power-law with index -1.15 .

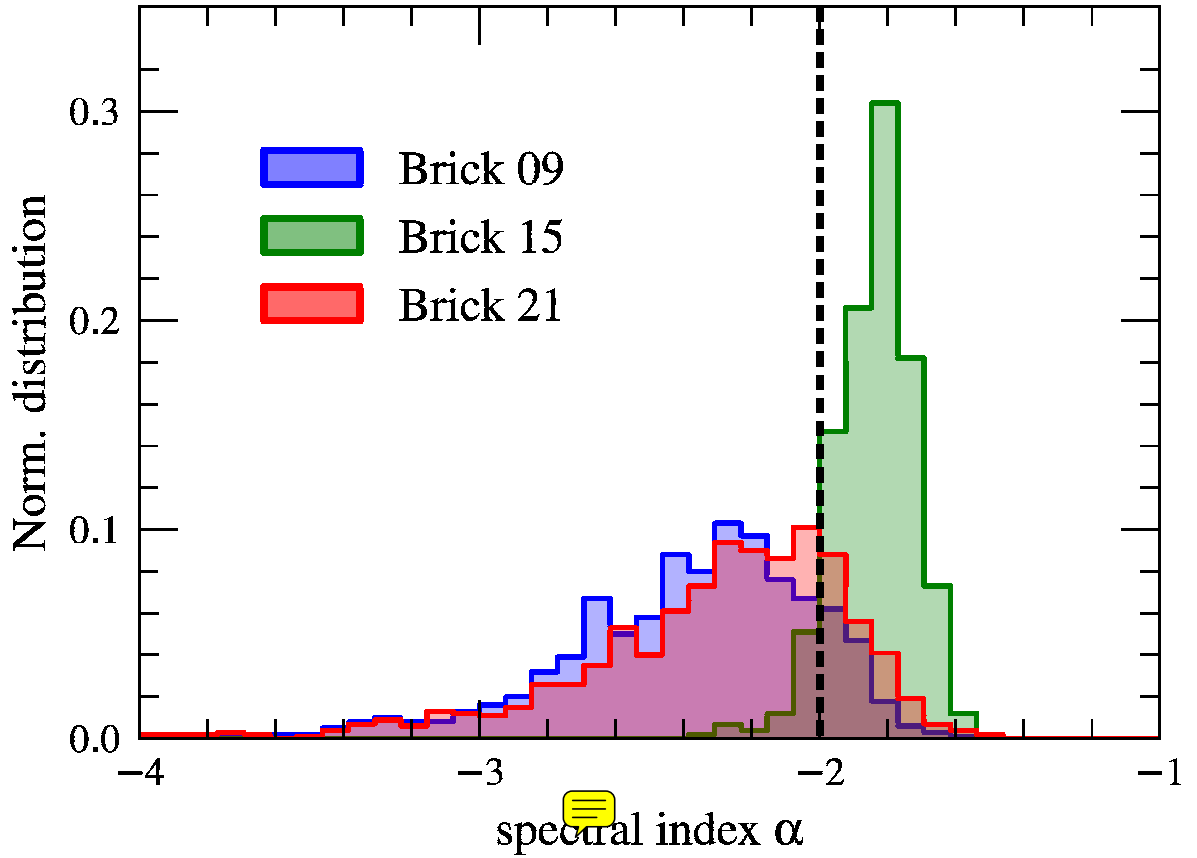


Fig. 9.— The distributions of the spectral indexes recovered from fitting a power-law to the mass distributions of the 3 outer regions in Fig. 7. The vertical dashed line indicates the canonical value of -2 .

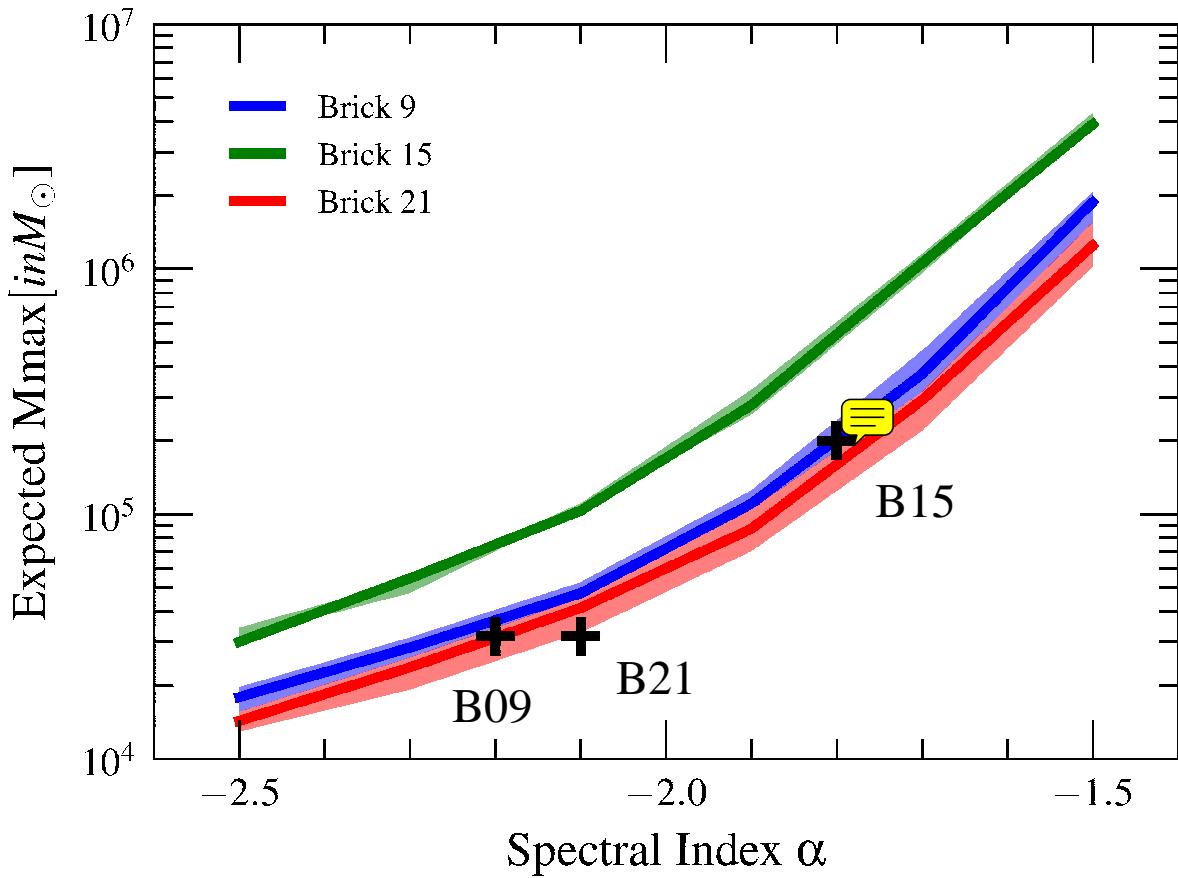


Fig. 10.— Distributions of expected most massive cluster mass as a function of the power-law spectral index, in each of the 3 outer regions of the study. Shaded regions are based upon the Poisson variations of the number of clusters per brick. Black crosses are the mass cut applied during the fit in §4.4 for the labeled regions.

REFERENCES

- Barbaro, C., & Bertelli, C. 1977, A&A, 54, 243
- Barton, E. J., Geller, M. J., & Kenyon, S. J. 2000, ApJ, 530, 660
- Bastian, N., & Gieles, M. 2008, in Astronomical Society of the Pacific Conference Series, Vol. 388, Mass Loss from Stars and the Evolution of Stellar Clusters, ed. A. de Koter, L. J. Smith, & L. B. F. M. Waters, 353–+
- Bastian, N., et al. 2011, MNRAS, 417, L6
- Bertelli, G., Bressan, A., Chiosi, C., Fagotto, F., & Nasi, E. 1994, A&AS, 106, 275
- Bik, A., Lamers, H. J. G. L. M., Bastian, N., Panagia, N., & Romaniello, M. 2003, A&A, 397, 473
- Billett, O. H., Hunter, D. A., & Elmegreen, B. G. 2002, AJ, 123, 1454
- Bohlin, R. C. 2007, in Astronomical Society of the Pacific Conference Series, Vol. 364, The Future of Photometric, Spectrophotometric and Polarimetric Standardization, ed. C. Sterken, 315
- Boutloukos, S. G., & Lamers, H. J. G. L. M. 2003, MNRAS, 338, 717
- Bressan, A., Fagotto, F., Bertelli, G., & Chiosi, C. 1993, A&AS, 100, 647
- Bruzual, G., & Charlot, S. 2003, MNRAS, 344, 1000
- Caldwell, N., Schiavon, R., Morrison, H., Rose, J. A., & Harding, P. 2011, AJ, 141, 61
- Cardelli, J. A., Clayton, G. C., & Mathis, J. S. 1989, ApJ, 345, 245
- Cerviño, M., & Luridiana, V. 2004, A&A, 413, 145

- Cezario, E., Coelho, P. R. T., Alves-Brito, A., Forbes, D. A., & Brodie, J. P. 2012, ArXiv e-prints
- Chandar, R., Fall, S. M., & Whitmore, B. C. 2006, ApJ, 650, L111
- . 2010, ApJ, 711, 1263
- Chiosi, E., Vallenari, A., Held, E. V., Rizzi, L., & Moretti, A. 2006, A&A, 452, 179
- Converse, J. M., & Stahler, S. W. 2011, MNRAS, 410, 2787
- Dalcanton, J. J., et al. 2012, ArXiv e-prints
- de Grijs, R., & Anders, P. 2006, MNRAS, 366, 295
- Di Matteo, P., Combes, F., Melchior, A., & Semelin, B. 2007, A&A, 468, 61
- Dowell, J. D., Buckalew, B. A., & Tan, J. C. 2008, AJ, 135, 823
- Efron, B. 1987, Journal of the American Statistical Association, 82, pp. 171
- Elmegreen, B. G., & Efremov, Y. N. 1997, ApJ, 480, 235
- Elmegreen, B. G., & Hunter, D. A. 2010, ApJ, 712, 604
- Fall, S. M., Chandar, R., & Whitmore, B. C. 2005, ApJ, 631, L133
- . 2009, ApJ, 704, 453
- Fioc, M., & Rocca-Volmerange, B. 1997, A&A, 326, 950
- Fouesneau, M., & Lançon, A. 2010, A&A, 521, A22
- Fouesneau, M., Lançon, A., Chandar, R., & Whitmore, B. C. 2012, ApJ, 750, 60
- Gieles, M., & Bastian, N. 2008, A&A, 482, 165

- Gieles, M., Heggie, D. C., & Zhao, H. 2011, MNRAS, 413, 2509
- Gieles, M., Lamers, H. J. G. L. M., & Portegies Zwart, S. F. 2007, ApJ, 668, 268
- Goodwin, S. P., & Bastian, N. 2006, MNRAS, 373, 752
- Groenewegen, M. A. T., & de Jong, T. 1993, A&A, 267, 410
- Hénon, M. 1961, Annales d’Astrophysique, 24, 369
- Hodge, P. 1987, PASP, 99, 724
- Hunter, D. A., Elmegreen, B. G., Dupuy, T. J., & Mortonson, M. 2003, AJ, 126, 1836
- Johnson, L. C., et al. 2012, ArXiv e-prints
- Kim, H., et al. 2012, ApJ, 753, 26
- King, I. 1962, AJ, 67, 471
- Kroupa, P., & Boily, C. M. 2002, MNRAS, 336, 1188
- Kroupa, P., Tout, C. A., & Gilmore, G. 1993, MNRAS, 262, 545
- Kruijssen, J. M. D., Pelupessy, F. I., Lamers, H. J. G. L. M., Portegies Zwart, S. F., & Icke, V. 2011, MNRAS, 414, 1339
- Kumai, Y., Basu, B., & Fujimoto, M. 1993, ApJ, 404, 144
- Lada, C. J., & Lada, E. A. 2003, ARA&A, 41, 57
- Lamers, H. J. G. L. M., Gieles, M., & Portegies Zwart, S. F. 2005, A&A, 429, 173
- Larsen, S. S. 2009, A&A, 494, 539
- Larsen, S. S., Origlia, L., Brodie, J., & Gallagher, J. S. 2008, MNRAS, 383, 263

- Larsen, S. S., & Richtler, T. 2000, A&A, 354, 836
- Lejeune, T., Cuisinier, F., & Buser, R. 1997, A&AS, 125, 229
- Maíz Apellániz, J. 2009, ApJ, 699, 1938
- McConnachie, A. W., Irwin, M. J., Ferguson, A. M. N., Ibata, R. A., Lewis, G. F., & Tanvir, N. 2005, MNRAS, 356, 979
- McCraday, N., & Graham, J. R. 2007, ApJ, 663, 844
- Meurer, G. R., Heckman, T. M., Leitherer, C., Kinney, A., Robert, C., & Garnett, D. R. 1995, AJ, 110, 2665
- Parmentier, G., & de Grijs, R. 2008, MNRAS, 383, 1103
- Piskunov, A. E., Kharchenko, N. V., Schilbach, E., Röser, S., Scholz, R., & Zinnecker, H. 2009, A&A, 507, L5
- Popescu, B., & Hanson, M. M. 2010, in IAU Symposium, Vol. 266, IAU Symposium, ed. R. de Grijs & J. R. D. Lépine, 511–515
- Portegies Zwart, S. F., McMillan, S. L. W., & Gieles, M. 2010, ARA&A, 48, 431
- Rafelski, M., & Zaritsky, D. 2005, AJ, 129, 2701
- Rubin, D. B. 1981, The Annals of Statistics, 9, pp. 130
- Searle, L., Wilkinson, A., & Bagnuolo, W. G. 1980, ApJ, 239, 803
- Spitzer, L. 1987, Dynamical evolution of globular clusters
- Vansevičius, V., Kodaira, K., Narbutis, D., Stonkutė, R., Bridžius, A., Deveikis, V., & Semionov, D. 2009, ApJ, 703, 1872

Whitmore, B. C., Chandar, R., & Fall, S. M. 2007, AJ, 133, 1067

Whitmore, B. C., & Zhang, Q. 2002, AJ, 124, 1418

Williams, B. F. 2003, AJ, 126, 1312

Zhang, Q., & Fall, S. M. 1999, ApJ, 527, L81

Zurita, A., & Bresolin, F. 2012, ArXiv e-prints

A. Comparison to continuous models

[MF: Still have to work on the figures and some text. I will add plots comparing best fits in ages and masses]

When relying on the integrated properties of clusters to determine ages and masses, the discreteness of the stellar mass function is an important limiting factor, especially for low-mass clusters. This is a typical issue in extragalactic studies, where the light from a $10^4 M_\odot$ cluster is dominated by on average only 3 or 4 supergiants (for ages up to a few 10 Myr). This means also that some will have no supergiants at all, while others will have more than the expected average. This leads to very large fluctuations in the integrated magnitudes and colors of clusters, which are complex and far from Gaussian distributions around the values predicted for a continuously populated mass functions (Barbaro & Bertelli 1977; Bruzual & Charlot 2003; Cerviño & Luridiana 2004; Maíz Apellániz 2009; Piskunov et al. 2009; Fouesneau & Lançon 2010; Popescu & Hanson 2010). Regardless of the limited validity of continuously populated mass function models, we repeated the

analysis of the PHAT cluster sample with the traditional approach to help comparisons with the existing literature.

The population synthesis assumptions are the same of as described above in §3.1, and the χ^2 calculation used to measure the quality of a fit is defined using fluxes as in the stochastic context (see Fouesneau & Lançon 2010, comparisons on synthetic data).

The two-dimensional (2D) age-mass distribution resulting from the “continuous” analysis is shown in Fig. 11. When compared to the results of the stochastic analysis, the distribution shows a less homogeneous distribution in age as Fouesneau & Lançon (2010) explained why this is expected. The “continuous” marginal distributions of cluster masses and cluster ages are compared to the stochastic ones in Fig. 12.

As already stated in the previous mentioned studies, the dip in the ”continuous” age distribution around 5×10^7 yr and the excessive accumulation of very young clusters are artifacts of that method. Regardless, of the two artifacts, the distributions tend to suggest the same cluster formation history: a relatively long period of formation decaying over the last 100 Myr.

The “continuous” marginal mass distribution is very close to the “discrete” homologue down to $10^3 M_\odot$. MF10 presented that continuous based analysis tend to under-estimate masses in this regime (especially for young clusters), which suggest that the expected peak at $10^3 M_\odot$ can be spread over lower mass bins. However, at such low mass regime, the mixture of completeness effects and the intrinsic limitations of the models makes it difficult to draw strong conclusions.

B. Catalog

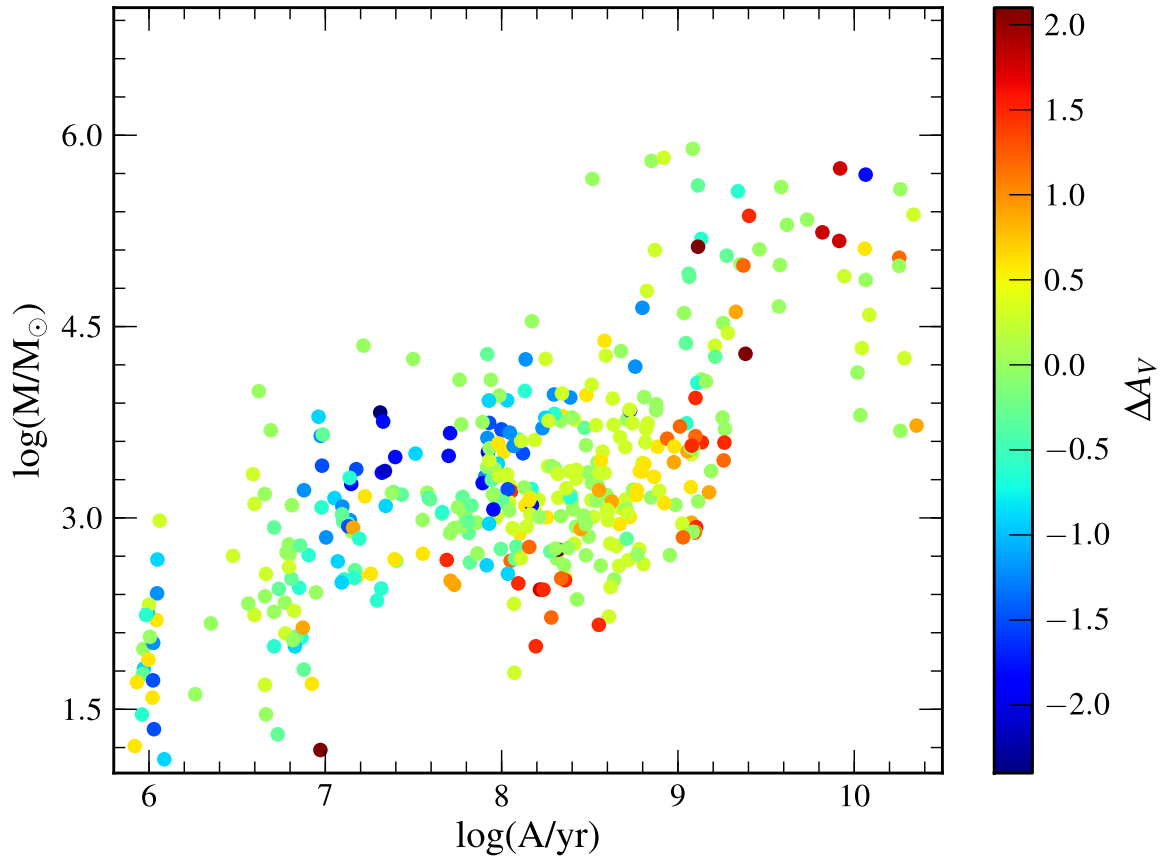


Fig. 11.— Age-mass distribution obtained from a χ^2 -fit using continuous models. Colors other than cyan and green highlight clusters for which the ages have changed most strongly between the continuous and the stochastic analysis (actually the scale is set by the corresponding change in AV).

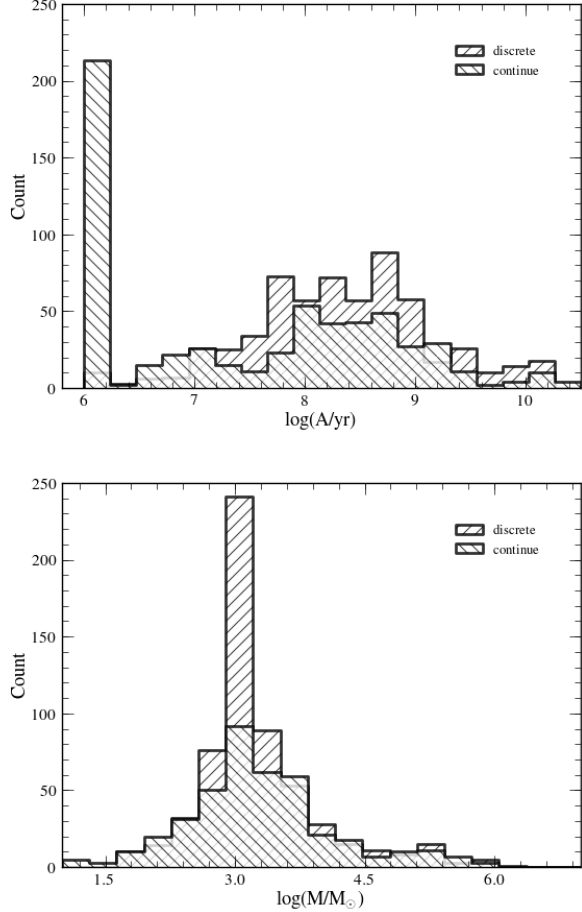


Fig. 12.— Comparing age and mass distributions (from the stochastic approach) and the traditional method (using the 6 filters available in PHAT) Age estimates are compared in the top panel, while mass estimates are compared in the bottom one. [**MF: will be changed for a more readable figure.**]